Electronic Supplementary Material (ESI) for Nanoscale.
This journal is © The Royal Society of Chemistry 2023

Supporting Information

Monocarboxylate-Protected Two-Electron Superatomic Silver Nanoclusters with High Photothermal Conversion Performance

Hao-Hai Wang [a†], Jianyu Wei [a,b†], Fahime Bigdeli [c†], Farzaneh Rouhani [c], Hai-Feng Su[d], Xiao-Ling Wang [a], Samia Kahlal [b], Jean-François Halet [b,e], Jean-Yves Saillard*[b], Ali Morsali*[c], and Kuan-Guan Liu*[a,d]

[a]Ningxia Key Laboratory for Photovoltaic Materials, School of Materials and New Energy, Ningxia University, Yinchuan, Ningxia 750021, China

[b]Univ Rennes, CNRS, Institut des Sciences Chimiques de Rennes (ISCR) – UMR 6226, F-35000 Rennes, France

[c]Department of Chemistry, Faculty of Sciences, Tarbiat Modares University, Tehran 14115175, Iran.

[d]State Key Lab of Physical Chemistry of Solid Surfaces, Department of Chemistry, College of Chemistry and Chemical Engineering, Xiamen University, 361005, China.

[e]CNRS–Saint-Gobain–NIMS, IRL 3629, Laboratory for Innovative Key Materials and Structures (LINK), National Institute for Materials Science (NIMS), Tsukuba, 305-0044, Japan.

† *These authors contributed equally to this work.*

Table S1. Crystal data and structural refinement for clusters **I**, **II**, **III** and **IV**

Compound	**I**	**II**	**III**	**IV**
CCDC No.	**2081489**	**2081416**	**2081417**	**2081420**
Chemical formula	$C_{324}H_{228}O_{26}P_8Ag_{16}$	$C_{324}H_{204}O_{24}P_8Cl_{24}Ag_{16}$	$C_{276}H_{176}O_{56}P_8Ag_{16}$	$C_{324}H_{228}O_{26}As_8Ag_{16}$
fw	6510.73	7305.13	6361.84	6862.33
Crystal system	Cubic	Trigonal	Trigonal	Cubic
Space group	Pa-3	R-3	R-3	Pa-3
a, Å	30.8121(5)	25.6949(11)	23.1930(3)	31.0591(2)
b, Å	30.8121(5)	25.6949(11)	23.1930(3)	31.0591(2)
c, Å	30.8121(5)	41.525(3)	42.6267(5)	31.0591(2)
α, deg	90	90	90	90
β, deg	90	90	90	90
γ, deg	90	120	120	90
V, Å^3	29252.6(14)	23742.97	19857.6(6)	29961.7(6)
Z	4	3	3	4
ρ_{calc}, g/cm^3	1.478	1.533	1.596	1.521
μ, mm^{-1}	1.151	1.268	10.336	1.958
Reflections collected	334174	13384	8010	92316
Independent reflections	11193	10021	5604	11454
R_{int}	0.0538	0.0439	0.0886	0.0803
Reflections I > 2σ(I)	11193	10021	5604	11454
Parameters	578	930	572	562
GOF on F^2	1.131	0.909	1.051	1.051
R_1[a] /wR_2[b] (I > 2σ(I))	0.0370/0.0942	0.082/0.2020	0.0767/0.1853	0.0454/0.1061
R_1[a] /wR_2[b] (*all*)	0.0411/0.0965	0.904/0.2232	0.1169/0.2021	0.0741/0.1170
Largest diff. peak and hole (e.Å^3)	1.751 and -0.581	1.67 and -1.24	1.472 and -0.944	0.505 and -1.576

[a] $R_1 = [\Sigma\ abs(abs(Fo) - abs(Fc))]/ [\Sigma\ abs(Fo)]$.

[b] $wR2 = [\Sigma(w(Fo^2 - Fc^2)^2)/ \Sigma[w(Fo^2)^2]^{0.5}$

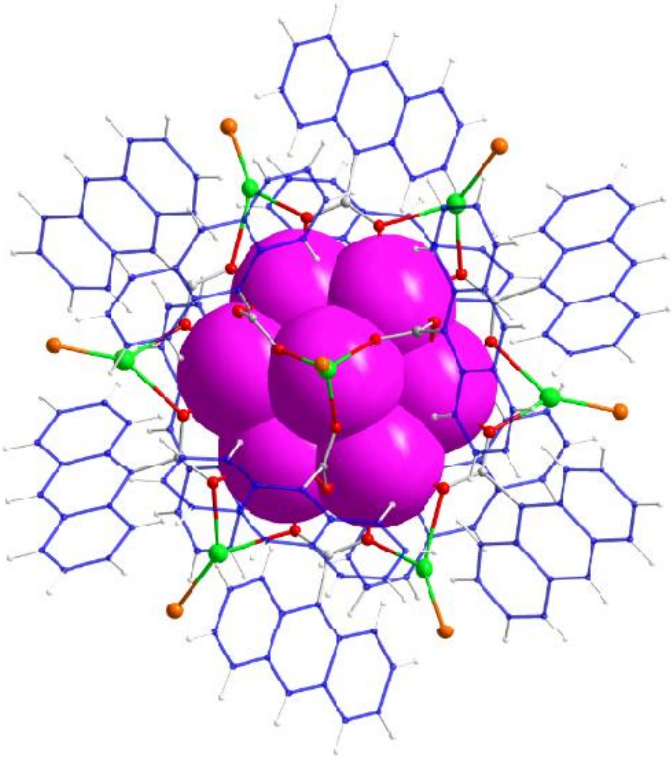

Figure S1. Presentation of the $Ag_8@Ag_8$ core-shell structure of the cluster $[Ag_{16}(L)_8(9\text{-}AnCO_2)_{12}]^{2+}$ [L = Ph_3P (**I**); $(4\text{-}ClPh)_3P$ (**II**); $(2\text{-}furyl)_3P$ (**III**); Ph_3As (**IV**)]. Color code: green, surface Ag; purple space-filling mode, kernel Ag; red, O; gray, C; blue, anthracene groups; gloden, phosphines or arsine ligands.

Table S2. Ag···Ag contact lengths [Å] for clusters **I- IV**

Cluster **I**		Cluster **II**		Cluster **III**		Cluster **IV**	
Ag(1)-Ag(1)$^{\#2}$	2.711(2)	Ag(2)-Ag(2)$^{\#3}$	2.839(5)	Ag(1)-Ag(1)$^{\#1}$	2.671(7)	Ag(1)-Ag(1)$^{\#2}$	2.715(3)
Ag(1)-Ag(1)$^{\#3}$	2.711(2)	Ag(2)-Ag(3)$^{\#4}$	2.896(2)	Ag(1)-Ag(1)$^{\#2}$	2.671(7)	Ag(1)-Ag(1)$^{\#1}$	2.715(3)
Ag(1)-Ag(3)$^{\#1}$	2.852(3)	Ag(2)-Ag(3)$^{\#5}$	2.897(2)	Ag(1)-Ag(2)	2.886(8)	Ag(1)-Ag(2)$^{\#3}$	2.854(4)
Ag(1)-Ag(3)	3.131(3)	Ag(2)-Ag(3)$^{\#3}$	2.897(2)	Ag(1)-Ag(2)$^{\#3}$	3.067(8)	Ag(1)-Ag(2)	3.131(4)
Ag(3)-Ag(3)$^{\#1}$	2.752(7)	Ag(2)-Ag(3)	3.033(2)	Ag(2)-Ag(2)$^{\#3}$	2.723(2)	Ag(2)-Ag(2)$^{\#3}$	2.742(10)

Table S3. Ag-O Bond lengths [Å] for clusters **I- IV**

Cluster **I**		Cluster **II**		Cluster **III**		Cluster **IV**	
Ag(1)-O(2)	2.357(2)	Ag(1)-O(3)	2.363(13)	Ag(1)-O(3)	2.306(6)	Ag(1)-O(3)	2.355(3)
Ag(1)-O(4)$^{\#1}$	2.362(3)	Ag(1)-O(3)$^{\#1}$	2.363(13)	Ag(1)-O(2)	2.341(7)	Ag(1)-O(2)$^{\#1}$	2.358(3)
Ag(1)-O(1)	2.484(2)	Ag(1)-O(3)$^{\#2}$	2.363(13)	Ag(1)-O(1)	2.438(7)	Ag(1)-O(1)	2.491(3)
Ag(2)-O(1)	2.267(2)	Ag(2)-O(3)	2.351(14)	Ag(2)-O(4)$^{\#4}$	2.340(7)	Ag(2)-O(4)$^{\#1}$	2.422(3)
Ag(2)-O(2)	2.397(2)	Ag(2)-O(3)$^{\#1}$	2.351(14)	Ag(2)-O(4)	2.340(7)	Ag(2)-O(4)$^{\#2}$	2.422(3)
Ag(3)-O(3)$^{\#4}$	2.432(2)	Ag(2)-O(3)$^{\#2}$	2.351(14)	Ag(2)-O(4)$^{\#5}$	2.340(7)	Ag(2)-O(4)$^{\#3}$	2.422(3)
Ag(3)-O(3)$^{\#5}$	2.432(2)	Ag(3)-O(2)	2.322(19)	Ag(3)-O(4)$^{\#4}$	2.345(8)	Ag(3)-O(1)	2.258(3)
Ag(3)-O(3)	2.432(2)	Ag(3)-O(1)$^{\#5}$	2.366(18)	Ag(3)-O(4)	2.345(8)	Ag(3)-O(2)$^{\#1}$	2.357(3)
Ag(4)-O(3)	2.359(2)	Ag(3)-O(4)$^{\#4}$	2.375(14)	Ag(3)-O(4)$^{\#5}$	2.345(8)	Ag(4)-O(4)	2.350(3)
Ag(4)-O(3)$^{\#4}$	2.359(2)	Ag(4)-O(1)	2.037(19)	Ag(4)-O(1)	2.221(7)	Ag(4)-O(4)$^{\#4}$	2.350(3)
Ag(4)-O(3)$^{\#5}$	2.359(2)	Ag(4)-O(2)$^{\#4}$	2.434(19)	Ag(4)-O(2)	2.353(7)	Ag(4)-O(4)$^{\#5}$	2.350(3)

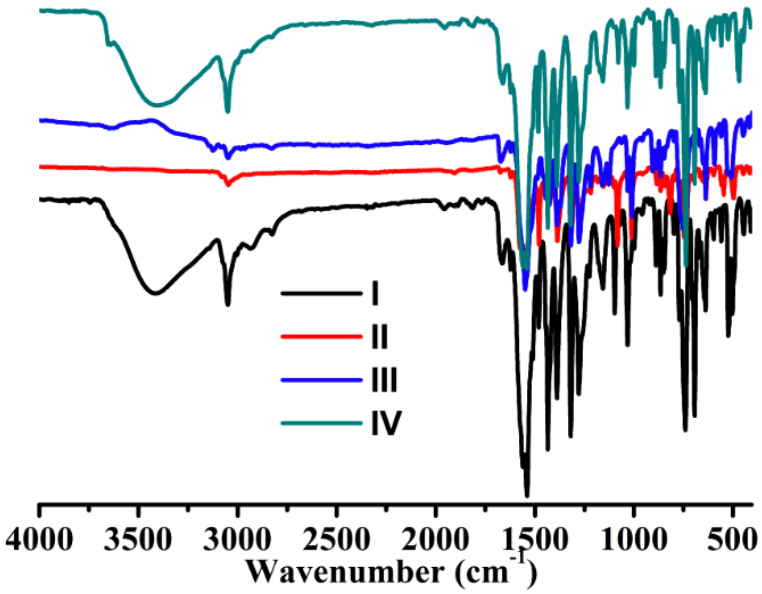

Figure S2. FT-IR spectra of the clusters **I- IV**

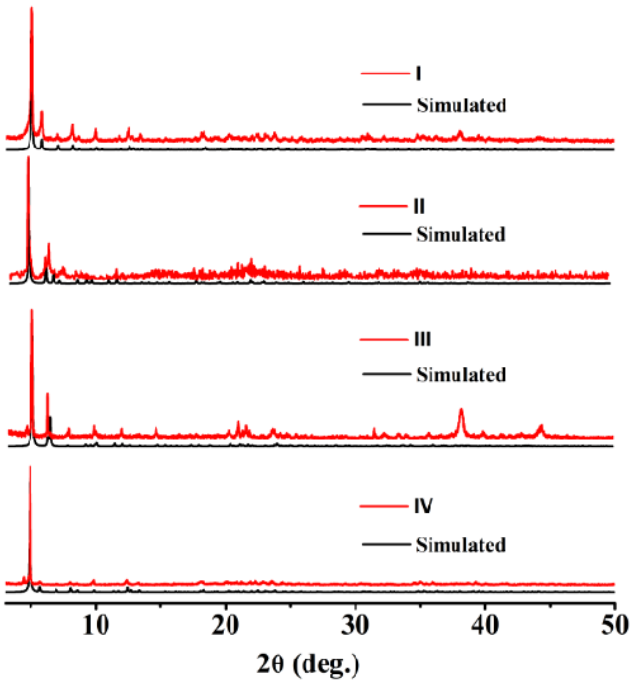

Figure S3. XRD patterns of the clusters **I- IV**

Table S4. Bond lengths [Å] for clusters **I- IV**

Cluster **I**		Cluster **II**		Cluster **III**		Cluster **IV**	
Ag(2)-P(1)	2.3625(8)	Ag(1)-P(1)	2.336(8)	Ag(3)-P(2)	2.322(4)	Ag(3)-As(1)	2.4414(6)
Ag(4)-P(2)	2.3297(14)	Ag(4)-P(2)	2.360(7)	Ag(4)-P(1)	2.332(3)	Ag(4)-As(2)	2.4147(10)

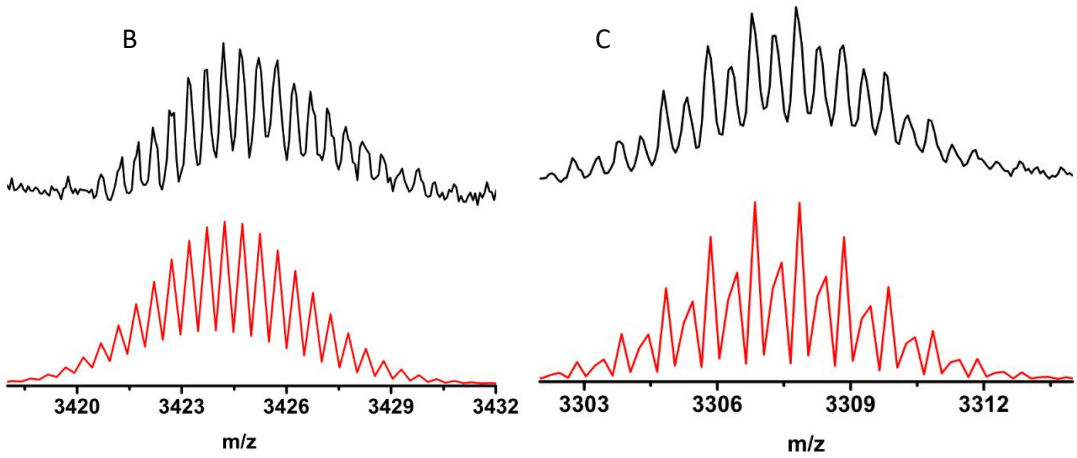

Figure S4. Presentation of the Zoom-in ESI-MS of the crystal **IV** dissolved in CH_3OH, experimental (blackline) and simulated (red line) isotopic patterns; Peak B centered at m/z = 3424.21 and Peak C centered at m/z = 3307.33, assigned to the formulas of $[M+H_2O]^{2+}$ (calculated m/z = 3424.28) and $[M-2Ag^0]^{2+}$ (calculated m/z = 3307.40), M = $[Ag_{16}(Ph_3As)_8(9\text{-}AnCO_2)_{12}]$ (**IV**).

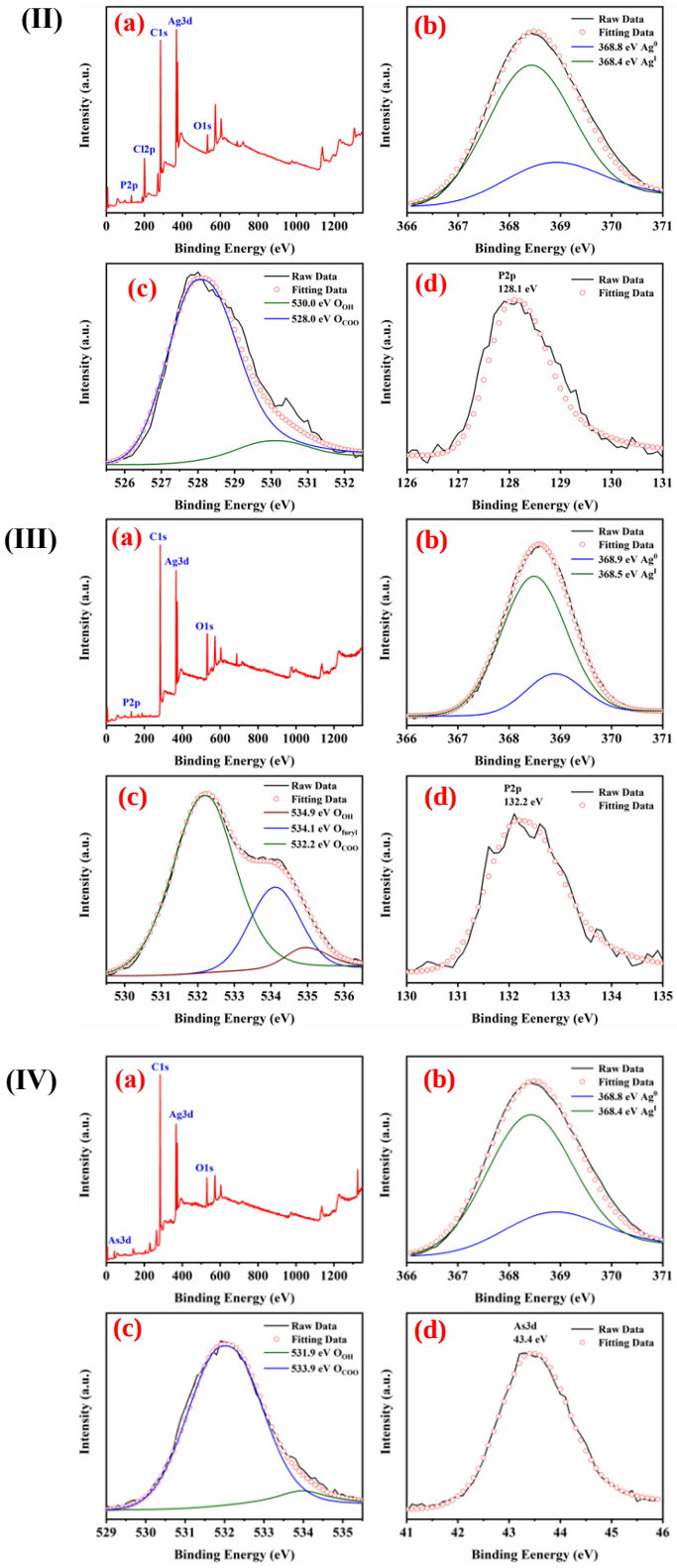

Figure S5. Full XPS spectra (a) and high-resolution XPS spectra [Ag3d (b), O1s (c), and P2p (d)] of nanocluster **II**; Full XPS spectra (a) and high-resolution XPS spectra [Ag3d (b), O1s (c), and P2p (d)] of nanocluster **III**; Full XPS spectra (a) and high-resolution XPS spectra [Ag3d (b), O1s (c), and As3d (d)] of nanocluster **IV**.

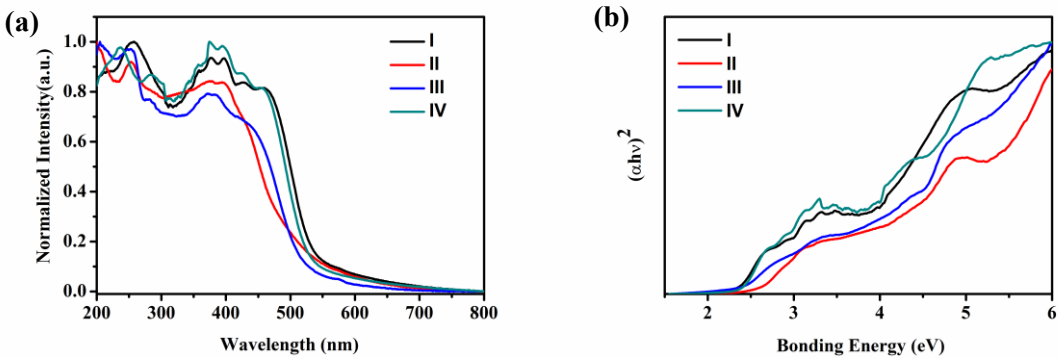

Figure S6. The solid-state UV-vis absorption spectra (a) and diffuse reflectance spectra (b) of the clusters **I-IV**.

I

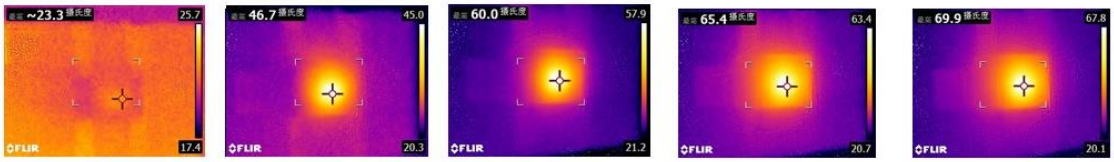

0 min (a) 1 min (b) 2 min (c) 3 min (d) 4 min (e)

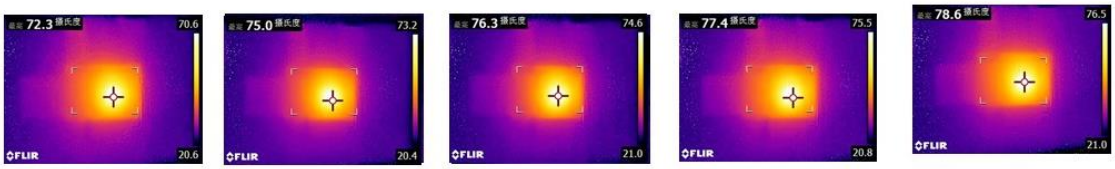

5 min (f) 6 min (g) 7 min (h) 8 min (i) 9 min (j)

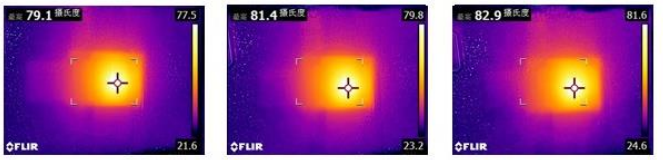

10 min (k) 20 min (l) 30 min (m) 60 min (n)

II

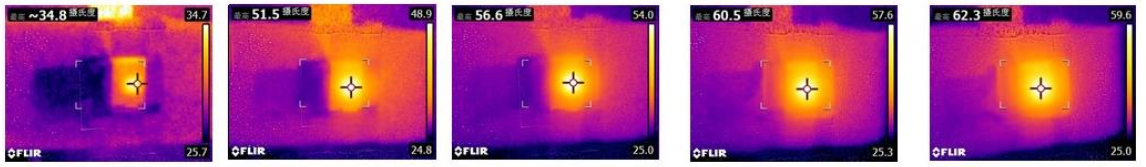

0 min (a) 1 min (b) 2 min (c) 3 min (d) 4 min (e)

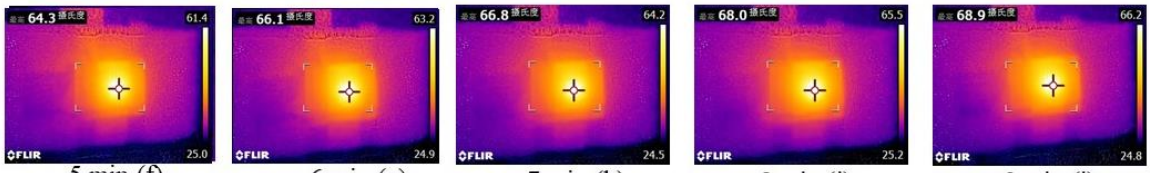

5 min (f) 6 min (g) 7 min (h) 8 min (i) 9 min (j)

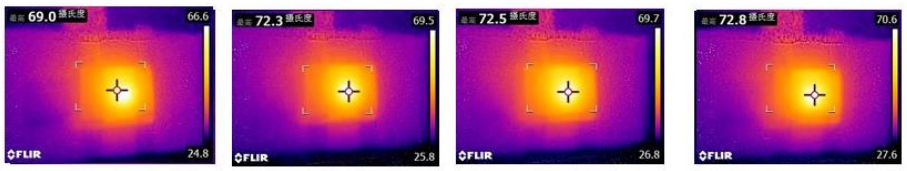

10 min (k) 20 min (l) 30 min (m) 60 min (n)

III

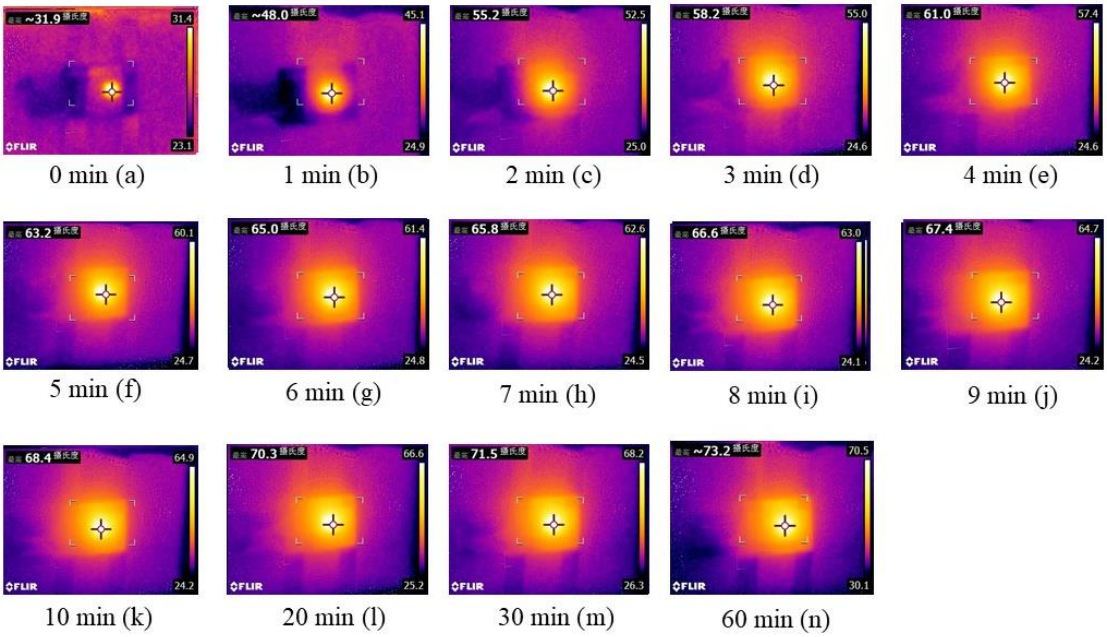

IV

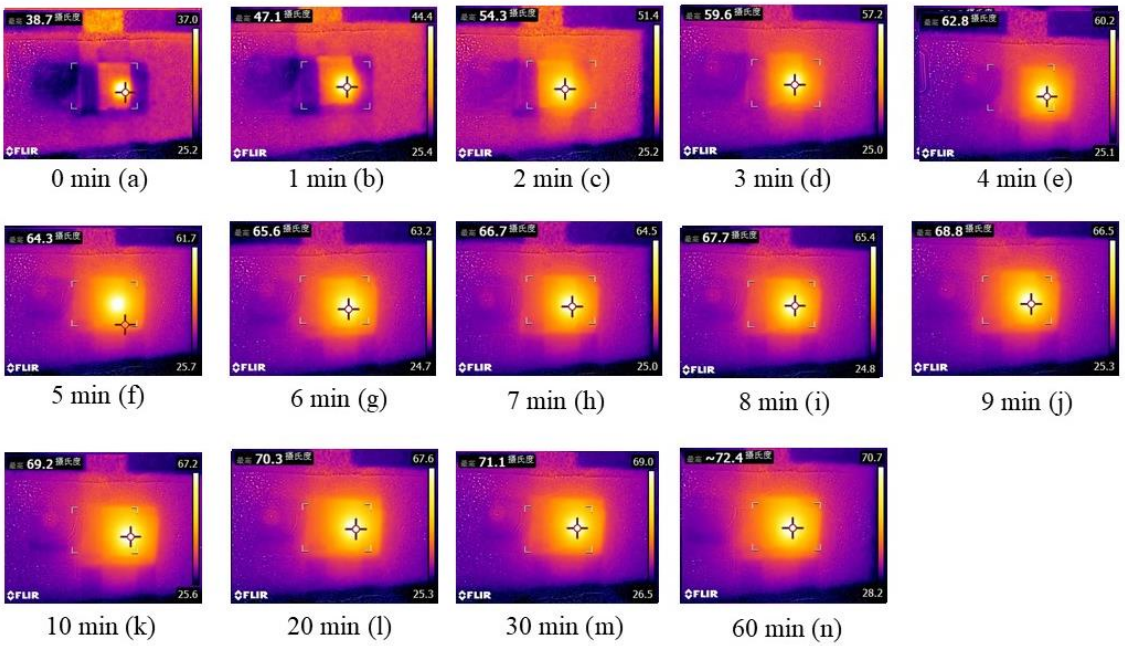

Figure S7. Temperature enhancement of the clusters **I- IV** over time due to light radiation.

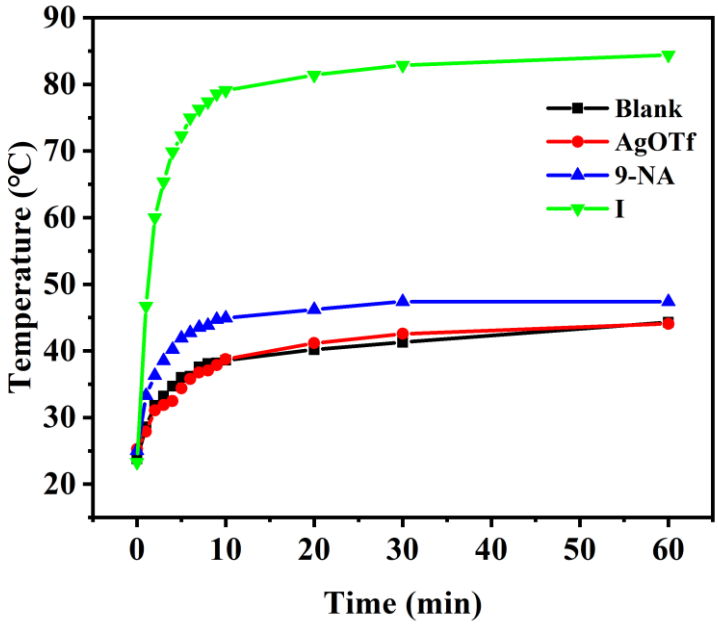

Figure S8. The temperature variation curves of the background (quzrtz glass), the metal precursors (AgOTf), the 9-Anthracene carboxylic acid ligand (9-NA) and cluster **I**.

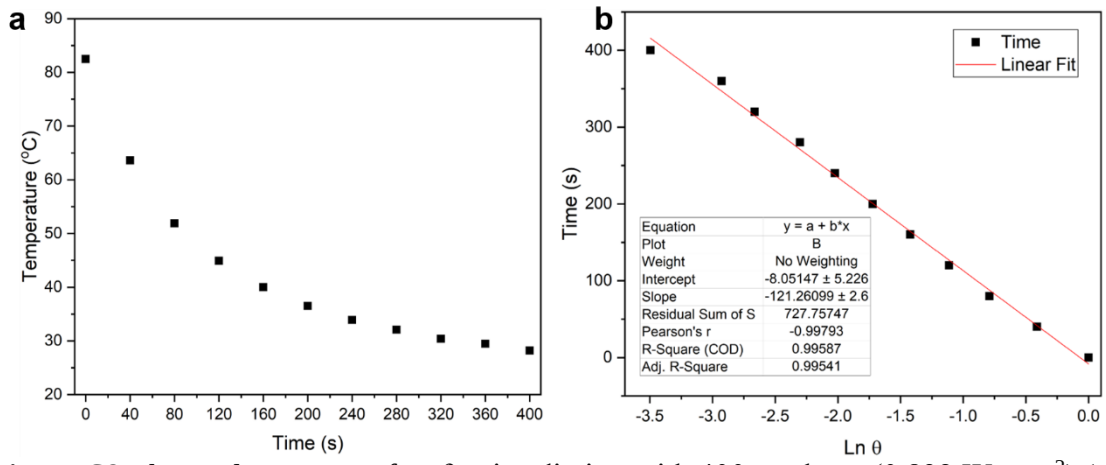

Figure S9 The cooling curve of **I** after irradiation with 400 nm laser (0.832 W· cm^{-2}) (**a**) and its corresponding time-lnθ linear curve (**b**).

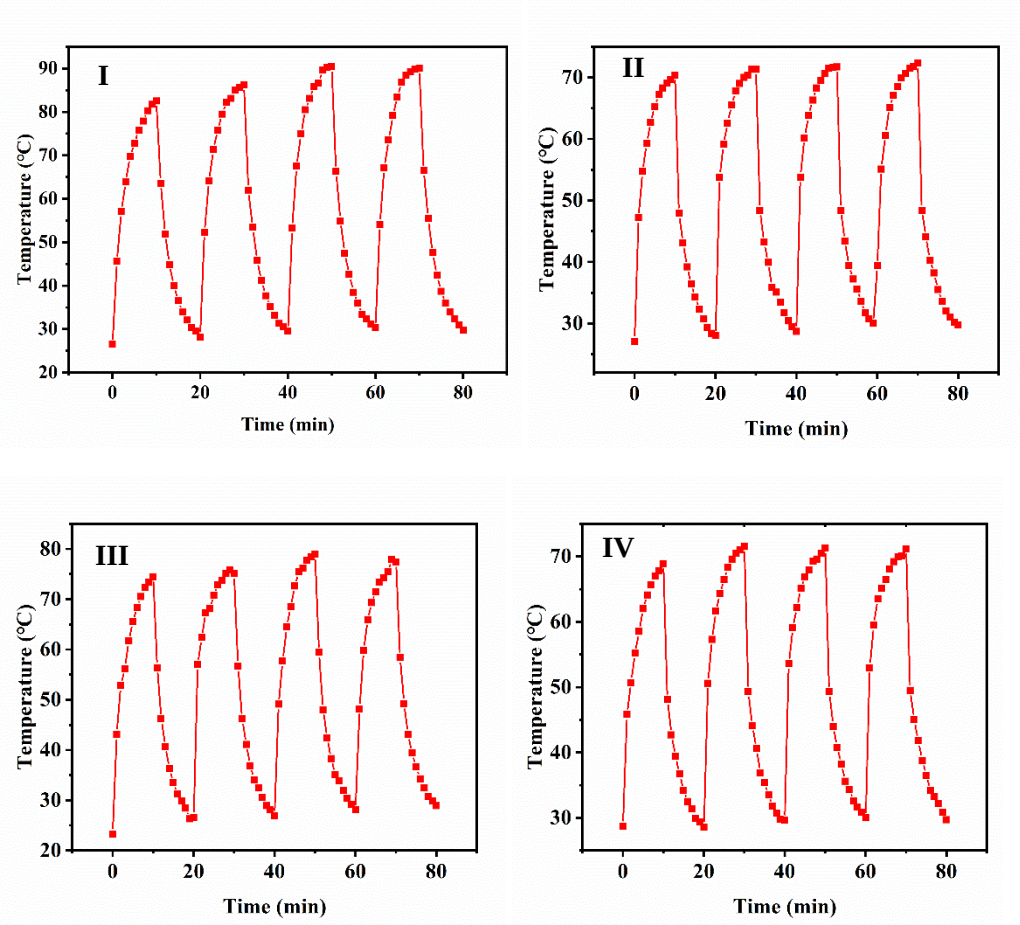

Figure S10. The temperature variation curves of nanoclusters **I-IV** for 4 photothermal cycles.

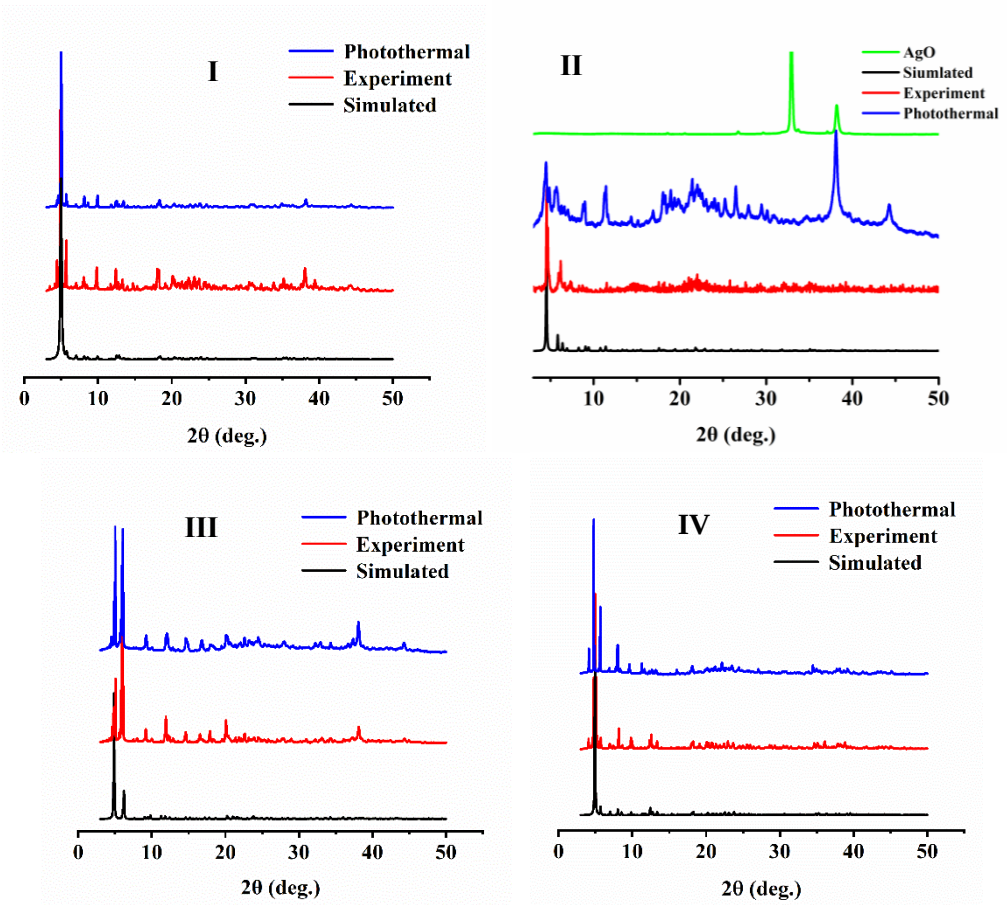

Figure S11. The XRD patterns of nanoclusters **I-IV** before and after 4 photothermal cycles.

Photothermal Conversion Efficiency

The photothermal conversion efficiency was calculated according to a previous method[1]. The calculations on the cluster **I** is shown as an example. Details are as follows:

Based on the total energy balance for this system:

$$\sum_i m_i C_{pi} \frac{dT}{dt} = Q_s - Q_{loss}$$

where m_i (0.81 g) and $C_{p,i}$ (0.8 J (g $^oC)^{-1}$) are the mass and heat capacity of system components (Cluster **I** and quartz glass), respectively. Q_s is the photothermal heat energy input by irradiating **I**, and Q_{loss} is thermal energy lost to the surroundings. When the temperature is maximum, the system is in balance.

$$Q_s = Q_{loss} = hS\Delta T_{max}$$

where h is heat transfer coefficient, S is the surface area of the container, ΔT_{max} is the maximum temperature change. The photothermal conversion efficiency η is calculated from the following equation:

$$\eta = \frac{hS\Delta T_{max}}{I(1 - 10^{-A_{400}})}$$

where I is the laser power (0.831 W cm^{-2}) and A_{400} is the absorbance of **I** at the wavelength of 400 nm (0.91).

In order to obtain the hS, a dimensionless driving force temperature, θ is introduced as follows:

$$\theta = \frac{T - T_{surr}}{T_{max} - T_{surr}}$$

where T is the temperature of **I**, T_{max} is the maximum system temperature (82.5 ^oC), and T_{surr} is the initial temperature (26.5 ^oC).

The sample system time constant τ_s

$$\tau_s = \frac{\sum_i m_i C_{p,i}}{hS}$$

thus $\frac{d\theta}{dt} = \frac{1}{\tau_s}\frac{Q_s}{hS\Delta T_{max}} - \frac{\theta}{\tau_s}$

when the laser is off, $Q_s = 0$, therefore $\frac{d\theta}{dt} = -\frac{\theta}{\tau_s}$, and $t = -\tau_s \ln\theta$

so hS could be calculated from the slope of cooling time vs $\ln\theta$. Therefore, τ_s is 121.26 s (Figure S9) and the photothermal conversion efficiency η is 41.1%.

Reference

1 B. Kim, H. Shin, T. Park, H. Lim and E. Kim, *Adv. Mater.*, 2013, **25**, 5483.